

**Advances in High-Harmonic Fast Wave Physics
in the National Spherical Torus Experiment**

G. Taylor, R.E. Bell, J.C. Hosea, B.P. LeBlanc, C.K. Phillips, M. Podesta,
E.J. Valeo, J.R. Wilson

Princeton Plasma Physics Laboratory, Princeton, New Jersey 08543, USA

J-W. Ahn, G. Ghen, D.L. Green, E.F. Jaeger, R. Maingi, P.M. Ryan, J.B. Wilgen
Oak Ridge National Laboratory, Oak Ridge, Tennessee 37831, USA

W.W. Heidbrink, D. Liu

University of California, Irvine, California 92697, USA

P.T. Bonoli

Plasma Science and Fusion Center, MIT, Massachusetts 02139, USA

T. Brecht

University of Minnesota, Minnesota 55455, USA

M. Choi

General Atomics, San Diego, California 92186, USA

R.W. Harvey

CompX, Del Mar, California 92014, USA

Abstract

High-harmonic fast wave (HHFW) heating and current drive are being developed in NSTX to provide bulk electron heating and $q(0)$ control during non-inductively sustained H-mode plasmas fuelled by deuterium neutral-beam injection (NBI), and to assist the plasma current ramp-up. Improved core HHFW heating, particularly at longer wavelengths and during low-density start-up and plasma current ramp-up, has now been obtained by lowering the edge density with lithium wall conditioning, thereby moving the critical density for perpendicular fast-wave propagation away from the vessel wall. Significant core electron heating of NBI-fuelled H-modes has been observed for the first time over a range of launched wavelengths. Visible and infra-red camera images of the antenna and divertor indicate that fast wave interactions can deposit considerable RF energy on the outboard divertor plate, especially at longer wavelengths that begin to propagate closer to the vessel walls. Edge power loss can also arise from HHFW-

generated parametric decay instabilities that drive ions in the edge onto direct loss orbits that intersect the wall, and may be the cause for an observed drag on edge toroidal rotation in combined HHFW and NBI discharges. During plasmas where HHFW is combined with NBI, there is a significant enhancement in neutron rate and fast-ion D_α emission measurements clearly show broadening of the fast-ion profile in the plasma core. Large edge localized modes (ELMs) have been observed immediately following the termination of RF power, whether the power turn off is programmed or due to antenna arcing. RF power has been successfully applied during large ELMs by setting the source reflection coefficient trip levels to relatively high values – an approach potentially important for ITER ICRF heating.

PACS# 52.55.Fa, 52.35.Hr

I. INTRODUCTION

Many magnetically confined fusion devices, including ITER, rely on radio-frequency (RF) heating and current drive (CD) to provide bulk heating and to control plasma stability. High-harmonic fast wave (HHFW) research in the National Spherical Torus (NSTX) [1] is directed towards maximizing the core heating and CD efficiency by reducing power loss between the antenna and the plasma edge. In particular, HHFW experiments and modeling are motivated by the need for core heating and $q(0)$ control during non-inductively sustained H-mode plasmas fuelled by energetic deuterium neutral-beam injection (NBI), as well as the need to provide HHFW-driven bootstrap current during solenoid-free plasma current ramp-up [2]. Recently, considerable progress has been made in improving the HHFW coupling and heating efficiency in Ohmically-heated helium and deuterium target plasmas, and in H-mode deuterium target plasmas heated and fuelled by deuterium NBI, and the results from this research may have particular significance for ITER [3].

The 12-strap HHFW antenna in NSTX is located on the outboard midplane and extends 90° toroidally. Six decoupled 30 MHz sources can provide up to 6 MW of radio-frequency (RF) power to the antenna. The antenna launches a well-defined spectrum of directed waves with launched toroidal wavenumbers, $k_\phi = \pm 13 \text{ m}^{-1}$, $\pm 8 \text{ m}^{-1}$ and $\pm 3 \text{ m}^{-1}$, when the phase difference ($\Delta\phi$) between adjacent antenna straps is $\pm 150^\circ$, $\pm 90^\circ$ and $\pm 30^\circ$, respectively [4, 5]. At other values of $\Delta\phi$ the antenna simultaneously launches several dominant spectral components. Lower k_ϕ waves should have higher CD efficiency, making $k_\phi = \pm 3 \text{ m}^{-1}$ particularly attractive for CD in NSTX.

NSTX plasmas typically have $\beta \sim 10\text{-}40\%$, resulting in strong single pass absorption of HHFW by electron Landau damping and transit-time magnetic pumping [1], even at the longest wavelengths that can be launched by the NSTX HHFW antenna (corresponding to $k_\phi = -3 \text{ m}^{-1}$). Both the GENRAY [6] ray tracing and the AORSA [7] full wave codes predict very strong first-pass absorption in the HHFW regime in NSTX [8, 9] with the waves being almost entirely damped as they pass through the high β core. Consequently, RF power losses in the plasma scrape-off and edge near the antenna play a critical role in limiting the heating efficiency in the plasma core. There are several

candidate processes that can contribute to RF power loss near the plasma edge; including parametric decay instability (PDI) heating via ion Bernstein wave excitation, and propagating and reactive wave-driven losses. It has also been observed in NSTX that when the edge density near the antenna is above the critical density for perpendicular fast wave propagation (n_{crit}) there is a reduction in core heating efficiency [8, 9] that is consistent with surface wave propagation near the antenna and the vessel wall, resulting in less RF power reaching the plasma core. A similar behavior is observed in conventional tokamaks at lower ICRF harmonics, where core heating efficiency is observed to be much lower with $\Delta\phi = 0^\circ$ phasing than with $\Delta\phi = 180^\circ$ [10]. n_{crit} is proportional $k_{||}^2 \times B/\omega$, where $k_{||}$ is the wavevector parallel to the magnetic field, B is the magnetic field and ω is the wave frequency. Earlier experiments on NSTX [8] had demonstrated improved HHFW heating efficiency in helium L-mode discharges by increasing B at the same k_ϕ [8]. Recently significant improvements in HHFW core heating efficiency were achieved by employing lithium conditioning [11] to reduce the edge density in order to move n_{crit} farther from the antenna and first wall [12, 13]. As a result the first clear observation of $k_\phi = -3 \text{ m}^{-1}$ core electron heating in deuterium was obtained. This is a particularly notable achievement because the CD efficiency is expected to be much higher at low k_ϕ . Lithium conditioning also resulted in record NSTX central electron temperatures, $T_e(0) > 5 \text{ keV}$ in deuterium and $> 6 \text{ keV}$ in helium with only 3 MW of $k_\phi = -8 \text{ m}^{-1}$ power. Lithium conditioning has also resulted in the first significant core electron heating of deuterium NBI-fuelled H-mode plasmas. Most notably, coupling of RF power was maintained through the L-mode to H-mode transition and was sustained even during H-modes with relatively large edge-localized modes (ELMs). These and other results obtained with lithium conditioning are presented in Section II.

Recently, visible camera images of the antenna and IR camera images of the lower divertor indicate that fast wave interactions can deposit considerable RF energy on the outboard divertor plate, especially for lower k_ϕ waves that begin to propagate closer to the vessel wall. Also, there is evidence that HHFW-generated PDI is heating ions in the edge and driving them onto direct loss orbits that intersect the wall, and that this process may be the cause for an observed drag on toroidal rotation near the plasma edge during

HHFW heating. During discharges with both HHFW and NBI heating there is an enhancement in the measured neutron rate, and fast-Ion D_α (FIDA) emission diagnostic data [14] clearly show significant broadening of the fast-ion profile near the plasma core during HHFW heating. These observations clearly show a strong interaction between fast-waves and fast-ions. The FIDA signals have recently been compared to signals simulated by the CQL3D Fokker-Planck code [15,16] and a full orbit simulation by the ORBIT-RF Monte-Carlo code [17]. Results on RF interactions with the plasma edge, divertor and fast-ions are presented in Section III. Recently the HHFW antenna was upgraded from a single to a double end-fed configuration. First results from this upgrade antenna show a higher arc-free power capability and are discussed in Section IV. A summary discussion of results and future plans is presented in Section V.

II. HHFW HEATING OF PLASMAS CONDITIONED WITH LITHIUM

Two lithium evaporators [11] that inject collimated beams of lithium towards the lower divertor applied lithium coatings to the graphite and carbon-fiber-composite plasma facing components in NSTX. These coatings have resulted in many beneficial effects [18], including contributing to improved HHFW electron heating in the plasma core by reducing the electron density in front of the antenna [13]. Figure 1 (a) shows the significant reduction in edge density, measured by multi-point laser Thomson scattering (MPTS), when lithium wall conditioning is added to deuterium plasmas heated by NBI. Two similar plasmas are compared, one with lithium conditioning (shot 129254, thick error bars and solid thick line) and one without lithium conditioning (shot 129239, thin error bars and dashed line). The reduction in edge density produced by lithium conditioning moves the n_{crit} away from the HHFW antenna, reducing surface wave coupling near the antenna and improving coupling to the plasma core. This has resulted in the production of plasmas with $T_e(0) > 5$ keV in deuterium and $T_e(0) > 6$ keV in helium with only ~ 3 MW of RF power. These temperatures are particularly impressive for NSTX which operates at a maximum axial toroidal field $B_T(0)$ of only 5.5 kG. Figures 1(b) – 1(e) show the electron density and temperature profiles measured by MPTS for two, $I_p = 650$ kA, $B_T(0) = 5.5$ kG, L-mode discharges that exhibit NSTX-

record core electron temperatures in helium (shot 135260) and deuterium (shot 129343). Figures 1(a) and 1(b) compare the electron temperature and density profile immediately prior to RF heating at 0.198 s (dashed line) and the profile during 2.7 MW of $k_\phi = -8 \text{ m}^{-1}$ ($\Delta\phi = -90^\circ$) heating at 0.298 s in a helium discharge. Figures 1(c) and 1(d) compare the electron temperature and density profile immediately prior to RF heating at 0.148 s (dashed line) and the profile during 3.1 MW of $k_\phi = -8 \text{ m}^{-1}$ heating at 0.248 s in a deuterium discharge. The T_e profiles became very peaked during RF heating, reaching $T_e(0) = 5.2 \text{ keV}$ in deuterium $T_e(0) = 6.2 \text{ keV}$ in helium. The T_e profile in deuterium is broader, with a steeper T_e gradient, probably due to the development of a reversed-shear q profile [19, 20]. The helium discharge eventually transitions to an H-mode plasma late in the RF heating pulse.

A scan of $\Delta\phi$ performed for series of deuterium L-mode plasmas with $I_p = 600 \text{ kA}$, $B_T(0) = 5.5 \text{ kG}$ that had 1 MW of RF power starting at 0.15s, and without using lithium conditioning, shows a degradation in heating efficiency with decreasing k_ϕ that is similar to the degradation measured in helium L-mode discharges [9]. $\Delta\phi$ was stepped from -180° to -30° in 30° increments, and included a plasma with no RF power. The results from the scan are summarized in Fig. 2. $T_e(0)$, measured by MPTS, (Fig. 2(a)) rises faster for larger $\Delta\phi$ (higher k_ϕ). Note for the shot with $\Delta\phi = -30^\circ$ ($k_\phi = -3 \text{ m}^{-1}$) there is an arc in the RF antenna at 0.22 s causing a notch in RF power. But even before the RF power notch it is clear the rise in $T_e(0)$ is almost the same as the shot with no RF power. Figures 2(b) and 2(c) show the T_e and n_e profiles measured by MPTS at 0.382 s. Larger $\Delta\phi$ (higher k_ϕ) results in a more centrally peaked T_e profile and lower $\Delta\phi$ results in higher $n_e(0)$.

Central electron heating at $k_\phi = -3 \text{ m}^{-1}$ in NSTX was only measured in deuterium plasmas when lithium wall conditioning was employed to reduce the edge density. Fig. 3 shows the $T_e(0)$ and $n_e L$ evolution measured by MPTS for two similar deuterium L-mode plasmas with 20 mg/min of lithium wall conditioning. Shot 129679 (solid lines) had up to 1.3 MW of $k_\phi = -3 \text{ m}^{-1}$ RF power (shaded region). Shot 129677 (dashed lines) had less than 150 kW of $k_\phi = -3 \text{ m}^{-1}$ RF power. There is a clear rise in $T_e(0)$ and $n_e L$ at each RF pulse in shot 129679 relative to shot 129677, although the heating efficiency in this case is still lower than at higher k_ϕ since the density at the antenna is still above n_{crit} .

Lithium conditioning has also enabled the first observation of significant HHFW central heating during an NBI-fuelled deuterium H-mode plasma. Earlier attempts to couple HHFW power into deuterium NBI-fuelled H-mode plasmas in NSTX, without the benefit of Li conditioning and at lower $B_T(0) = 4.5$ kG, resulted in edge ion heating, but no core heating [21]. Figure 4 shows (a) $T_e(R)$, (b) $n_e(R)$ and (c) $P_e(R)$ measured by MPTS at 0.482 s for two $I_p = 1$ MA, $B_T(0) = 5.5$ kG deuterium plasmas. One plasma had 2 MW of NBI and 1.6 MW of RF power, with $\Delta\phi = 180^\circ$ ($k_\phi = (14 + 18) \text{ m}^{-1}$), from 0.3 to 0.5 s (thick solid line, shot 129386), and the other plasma had 2 MW of NBI from 0.09 to 0.69 s (thin dashed line, shot 129381). There is a significant increase in $T_e(0)$ and $P_e(R)$ during the RF heating pulse. $\Delta\phi = 180^\circ$ antenna phasing launches about the same power in each toroidal direction, so while it heats the plasma it cannot be used for driving current, for example to control $q(0)$.

The results shown in Fig. 4 were obtained with the benefit of mostly residual lithium coatings and minimal freshly deposited lithium. H-mode plasmas heated by NBI, and conditioned with fresh lithium conditioning sustained throughout the discharge, have been heated with 1.8 MW of $k_\phi = -13 \text{ m}^{-1}$ and $k_\phi = -8 \text{ m}^{-1}$ power (antenna launch spectra that can both heat and drive current). Electron heating was shifted off-axis and less heating was measured at $k_\phi = -8 \text{ m}^{-1}$ than at $k_\phi = -13 \text{ m}^{-1}$, similar to the heating efficiency trend measured in L-mode plasmas. About 66% of the RF power (~ 1.2 MW) was estimated to couple to the plasma at $k_\phi = -13 \text{ m}^{-1}$, and about 40% (~ 0.7 MW) was coupled at $k_\phi = -8 \text{ m}^{-1}$. MPTS edge density data indicate that the edge density was below n_{crit} for the case with $k_\phi = -13 \text{ m}^{-1}$ heating but it was above n_{crit} for the case with $k_\phi = -8 \text{ m}^{-1}$ heating. Figure 5(a) shows the time history of the plasma stored energy for the case with $k_\phi = -13 \text{ m}^{-1}$ heating (shot 130608, solid black line) compared to a similar plasma with no RF heating (shot 130609, dashed black line). The RF pulse on shot 130608 turns off three times, the first two times because of an antenna arc (0.375 s and 0.437 s) and the third time during a programmed RF pulse shutdown (0.5 s). There is a clear rise in plasma stored energy during each RF pulse and at the end of each RF pulse there is a large type 1 ELM, indicated by the spike in divertor D_α emission (red line). Figure 5(b) shows an enlarged time window around the time of the arc at 0.375 s, the large ELM clearly follows the turn off of the RF pulse. Similarly, Fig. 5(c) shows the

large ELM following the programmed RF turnoff follows the shut down of the RF power. Fast camera images prior to the growth of the ELM do not show the usual helical ELM structure [12], suggesting that the ELM may be caused by the relaxation of the edge pressure, energetic ion population or current profile after the RF power turns off.

A challenge for coupling HHFW to H-mode plasmas is to maintain good coupling through the L-H transition and large ELMs that can significantly modify the edge density profile and change the separation between the antenna and the n_{crit} location. This can in turn lead to large changes in reflected power that can exceed the RF reflection coefficient trip level (typically set to 60-70% of the forward RF power) shutting down the RF sources. The issue here is not that 100% reflected power would damage the RF sources, but rather that there is a need to discriminate between reflections due to coupling issues outside the antenna and arcs in the antenna that could potentially lead to serious damage. Fig. 6 shows data from an $I_p = 800$ kA, $B_T(0) = 5.5$ kG deuterium plasma (shot 135340), conditioned with lithium, that was initially heated by 2 MW of NBI. 2.7 MW of $k_\phi = -13$ m⁻¹ heating was applied from 0.25 to 0.46 s and an L-H transition occurs soon after the start of the RF pulse at 0.29 s. Fig. 6(a) shows the drop in divertor D_α emission at the time of the L-H transition followed by a sequence of D_α spikes during the ELMs. In this case RF power is sustained through the L-H transition and the ELMs. Figs. 6(b) and (c) show MPTS $P_e(R)$ and $n_e(R)$ profiles at three times, just before (0.282 s) and after (0.298 s) the L-H transition and near the end of the RF pulse (0.432s). The edge density profile rapidly steepens at the L-H transition and the $P_e(R)$ doubles during the RF pulse. Fig. 6(d) shows the RF reflection coefficient (blue) overlaid on the RF power waveform (black) and the divertor D_α signal (red). While there are large fluctuations in the reflection coefficient it only exceeds 30% briefly at the L-H transition and never approaches the trip level.

Lithium wall conditioning also improves HHFW coupling during discharge startup and early plasma current ramp-up. This is particularly important because in solenoid-free spherical torus scenarios, HHFW-generated bootstrap current ramp-up to $I_p > 400$ kA is needed to provide sufficient current to confine NBI ions in NSTX [2]. Recent experiments have successfully coupled $k_\phi = -8$ m⁻¹ power into lithium-conditioned deuterium plasmas at very low $T_e(0)$ and I_p . 550 kW of RF power has been

coupled between 9 and 22 ms during the initiation of a discharge by Coaxial Helicity Injection (CHI) [22], increasing $T_e(0)$ from 3 to 15 eV when $n_e(0) \sim 4 \times 10^{18} \text{m}^{-3}$. 550 kW of $k_\phi = -8 \text{ m}^{-1}$ power was also coupled 20 to 64 ms into the I_p ramp following CHI. Figure 7 shows (a) $T_e(R)$, (b) $n_e(R)$ and (c) $P_e(R)$ measured by MPTS at 52 ms for a the plasma with RF power (solid black line) and a similar plasma without RF power (dashed black line). With the addition of RF power $T_e(0)$ increased from 3 to 33 eV, $n_e(R)$ broadened and $n_e(0)$ increased by about 20%. As a result $P_e(0)$ increased by about an order of magnitude, although $P_e(R)$ remained hollow.

III. RF INTERACTION WITH PLASMA EDGE, DIVERTOR AND FAST-IONS

While surface wave losses can be reduced by edge conditioning techniques, such as lithium wall coatings, there is evidence of other detrimental RF power loss processes, particularly at lower k_ϕ . Previous passive spectroscopic ion temperature measurements for helium plasmas by the edge rotation diagnostic (ERD) [23] on NSTX indicated that PDI ion heating by ion Bernstein wave (IBW) excitation may account for the loss of 16-23% of the RF power through ion collisions with poorly-confined edge electrons [24]. But the direct loss of PDI-generated energetic ions in the plasma edge may also be a significant loss channel for RF power. PDI-generated edge ion heating of carbon-III was measured during a sequence of similar $I_p = 650 \text{ kA}$, $B_T(0) = 5.5 \text{ kG}$ deuterium discharges with 1.2-1.3 MW of RF heating in which k_ϕ was changed from -13 m^{-1} to -3 m^{-1} . The poloidal edge ion temperature near the plasma separatrix ($R \sim 1.5 \text{ m}$) was measured to increase with decreasing k_ϕ , as shown in Fig. 8(a). The ion heating became increasingly anisotropic as k_ϕ was reduced, with no change in toroidal ion temperature as k_ϕ was changed (Fig. 8(b)). Similar edge ion heating behavior was seen for carbon-VI, helium-II and lithium-II. The carbon-III poloidal ion temperature (Fig. 8(c)) and emissivity peaked at the plasma separatrix, whereas the carbon-III toroidal emissivity peaked outside the plasma separatrix, as shown in Fig. 8(d). A 1-D full wave model [25] was used to simulate the dependence of the amplitude of the PDI-generated IBW on the RF power for the range of k_ϕ values used in the experiment, and the results are summarized in Fig. 8(e). The model predicts that the threshold for PDI should fall with decreasing

k_ϕ , as seen in the experiment. The model also predicts that significant PDI should be generated with only 100 kW of RF power at $k_\phi = 3 \text{ m}^{-1}$ and $\sim 250 \text{ kW}$ at $k_\phi = 13 \text{ m}^{-1}$.

Other evidence for the direct loss of PDI-generated energetic ions in the plasma edge is provided by charge exchange recombination spectroscopy (CHERS) [26] measurements of the plasma toroidal rotation velocity (V_{tor}). CHERS data were measured during a 40 ms 2 MW NBI pulse which overlapped the end of the RF heating pulse by 30 ms during the antenna $\Delta\phi$ scan shown in Fig. 2. The CHERS measurements for carbon-VI V_{tor} at $R = 1.45 \text{ m}$, just inside the plasma separatrix, during the antenna $\Delta\phi$ scan are summarized in Fig. 9(a). The edge V_{tor} slows down more at lower $\Delta\phi$ (k_ϕ) and after the RF power is turned off V_{tor} immediately increases. Figure 9(b) shows the carbon-VI V_{tor} profiles measured by CHERS for the shot with $\Delta\phi = -60^\circ$. The profiles marked “10 ms”, “20 ms” and “30 ms” are measured when the RF is still turned on. V_{tor} begins to increase as the NBI imparts toroidal rotation to the core of the plasma, but V_{tor} near the edge remains clamped until the RF power is turned off, as indicated by the profile marked “40 ms”. The black curve with the solid circles is the projected V_{tor} profile before the NBI pulse was turned on. The CHERS data suggests that ions are gaining perpendicular energy from the PDI [23] and are then being ejected into the plasma scrape-off, increasing the electric field and changing ExB shear in the edge.

As mentioned in the previous section, there are evidently significant edge RF power losses occurring in HHFW-heated H-mode plasmas, even with the benefit of lithium wall conditioning. At $k_\phi = -13 \text{ m}^{-1}$ about a third of the RF power is estimated to be lost before it can couple to the core plasma and this loss increases to about two-thirds for $k_\phi = -8 \text{ m}^{-1}$ heating. While PDI-related mechanisms may account for some of this RF power loss it seems likely that there is a significant additional fast-wave power loss mechanism occurring. Evidence for the existence of this mechanism is provided by visible color and infrared camera measurements, as summarized in Fig. 10. Figures 10(a-c) show visible color camera images taken during three $I_p = 1 \text{ MA}$, $B_T(0) = 5.5 \text{ kG}$ deuterium H-mode plasmas. Image (a) had only 2 MW of NBI heating (shot 130609). Images (b) and (c) had 2 MW of NBI heating and 1.8 MW of $k_\phi = -8 \text{ m}^{-1}$ heating (shot 130621) and 1.8 MW $k_\phi = -13 \text{ m}^{-1}$ heating (shot 130608), respectively. The images in frames (b) and (c) were taken at 0.335 s. Image (a) was taken at 0.350 s. An NBI-only

background frame at 0.250 s in each shot was subtracted from each image. When RF heating is applied RF power flows along the magnetic field lines onto the lower outer divertor plate, and this flow becomes much more prominent for the case with $k_\phi = -8 \text{ m}^{-1}$ heating (Fig. 10(b)) than for the case with $k_\phi = -13 \text{ m}^{-1}$ heating (Fig. 10(c)). Recently, dramatic evidence of the power densities associated with this interaction has been provided by calibrated infrared camera measurements of the lower divertor plates. Fig. 10(d) shows a plot of the heat flux versus major radius for two H-mode plasmas, both with 2 MW of NBI (black dashed line) and one with 2.6 MW of $k_\phi = -8 \text{ m}^{-1}$ heating (red solid line). The heat flux to the lower outer divertor plate increases by about a factor of six, to $3 \text{ MW}\cdot\text{m}^{-2}$ when RF heating is applied.

GENRAY [6] modeling of the power deposition and partitioning between ions and electrons has been performed for recent deuterium HHFW + NBI H-mode discharges in NSTX. Results of this modeling are summarized for $k_\phi = -8 \text{ m}^{-1}$ (shot 130621) and $k_\phi = -13 \text{ m}^{-1}$ (shot 130608) heating in Fig. 11. The results shown in Fig. 11 use the effective temperature and density for slowing NBI deuterium ions produced from TRANSP [27] time-dependent transport analysis of shot 130609, which is similar to shots 130608 and 130609, but without RF heating. RF power turns on at 0.25 s in shots 130608 and 130621 and the GENRAY analysis is performed at 0.353 s. At that time, in the case with $k_\phi = -8 \text{ m}^{-1}$ heating about 70% of the RF power is deposited on electrons and 30% is deposited on fast-ions (Fig. 11(a)). In the case with $k_\phi = -13 \text{ m}^{-1}$ heating about 85% of the RF power is deposited on electrons and 15% is deposited on fast-ions (Fig. 10(a)). When an NBI fast-ion population is not included in the GENRAY modeling over 95% of the RF power is predicted to couple to electrons for both RF cases. It is important to note here that the GENRAY modeling does not include RF acceleration of fast-ions. A TORIC [28] implementation in TRANSP, that does not include a self-consistent treatment of the change in fast-ion population due to the RF acceleration, shows a strong competition between electron and fast-ion damping in HHFW+NBI discharges that changes dynamically in time. A TORIC-TRANSP analysis of shot 130608 predicts half the RF power is damped on fast-ions at the start of the RF pulse (0.25 s), but this falls to about 40% at the time of the GENRAY analysis (0.353 s)

shown in Fig. 11(b). [GT: Maybe something on comparison between GENRAY, AORSA and TORIC from Cynthia]

Much of the RF power deposited on fast-ions in the core is expected to result in scattering of the ions into the banana loss region in the outer two-thirds of the plasma, so it is important to directly measure the spatial changes in the fast-ion profile in the presence of HHFW. There have been numerous studies of the interaction between fast-waves and fast-ions [29-33], however most of these studies were performed at fundamental or low ion cyclotron harmonics. Previously HHFW acceleration of NBI fast-ions was only studied in NSTX with neutron counters and an E//B neutral particle analyzer (NPA) [33], which yielded almost no data on the spatial interaction between the fast-waves and the fast-ion population. With the installation of the FIDA [14] diagnostic and solid-state NPA (SSNPA) array [34] on NSTX it has been possible to measure the change in spatial distribution of fast-ions during HHFW heating [16]. Figure 12(a-c) shows waveforms from a sequence of deuterium plasmas with 65 keV NBI blips (Fig. 11(a)). A 1.1 MW $k_{\phi} = -8 \text{ m}^{-1}$ RF pulse is coupled from 0.15 to 0.4 s (Fig. 12(b)). Neutron measurements show a clear enhancement due NBI fast-ion acceleration when shots with and without RF are compared (Fig. 12(c)). Figure 12(d) shows a plot of the FIDA signal measured between 0.29 and 0.36s for three shots with RF (red line and symbols) and one shot with no RF (black line and symbols). There is a factor of two enhancement in the FIDA signal in the shot with RF power. [GT: Maybe something on comparison with CQL3D and ORBIT RF]

IV. RECENT RESULTS FROM THE DOUBLE END-FED ANTENNA

Until the 2009 experimental campaign the NSTX 12-strap HHFW antenna had been coupled to the six RF transmitters by 12 antenna feeds connected to the top of each antenna strap [4, 5]. The bottom of each strap was connected to ground. Vacuum conditioning of the antenna in this configuration typically reached a voltage limit $\sim 25 \text{ kV}$, but when coupling to plasma the system voltage limit was typically $\sim 15 \text{ kV}$. If the mechanism limiting system voltage during plasma operation is the electric field in the vicinity of the straps and Faraday shield then it should be possible to increase the

system voltage limit during plasma operation towards the vacuum voltage limit by reducing the electric field at the straps. To accomplish this the straps were reconfigured with a ground in the center of each strap and a transmission line feed to both the top and bottom of each strap. This reconfiguration included installing new antenna straps and entailed adding half-wavelength loops (~5 m long) between the top and bottom antenna feeds on each strap. These modifications, plus increasing some critical gaps by ~ 20-25%, were expected to reduce electric fields on the straps by about a factor of two and in the antenna box by about a factor of 1.4. Modifications to the transmission line components external to the vacuum vessel were accomplished during the early months of the 2009 run campaign when large amounts of lithium were being coated on internal vessel hardware, including the antenna. The upgraded antenna was operated during the last six weeks of the campaign, after several months of lithium-conditioned plasma operation. Initially the voltage limit for operation into vacuum was below 10 kV, but quickly increased to about 25 kV. Fast visible camera observations of the antenna during vacuum conditioning indicated that breakdowns were occurring in the antenna box, not in the transmission lines. When HHFW plasma operation began with the upgraded antenna it achieved the previous RF power levels (2-3 MW) more quickly than during previous campaigns. Figure 13 shows fast TV camera images of material being ejected, including lithium, from the boron nitride between the straps, and at the top and bottom of the antenna. Figure 13(a) is an image of the antenna showing strap locations under uniform plasma illumination. The camera images straps 1 through 9. Figures (b) and (c) show material being ejected from between straps 7 and 8 at the bottom of the antenna from the top of the antenna between straps 7, 8 and 9. Arcs in the antenna correlated with these ejections. Arcs probably occur when particles enter the high field region inside the antenna Faraday shield. However, many ejection events are not accompanied by arcing.

The plasma performance was significantly improved over previous run campaigns. Over 4 MW was coupled into a helium L-mode plasma, $T_e(0) > 6.2$ keV was achieved with only 2.7 MW of RF power and HHFW coupling was maintained through the L-H transition and during relatively large ELMs during deuterium NBI-fuelled H-mode discharges. The improved performance and reliability of the new antenna also allowed a

detailed study of the L-H and H-L transition in helium and deuterium plasmas heated only by Ohmic and HHFW heating.

V. SUMMARY DISCUSSION AND FUTURE WORK

Improved core HHFW heating, particularly at longer wavelengths and during low-density start-up and plasma current ramp-up, has now been obtained by lowering the edge density with lithium wall conditioning. Significant core electron heating of NBI-fuelled H-modes has been observed for the first time over a range of launched wavelengths.

Visible and infra-red camera images of the antenna and divertor indicate that fast wave interactions can deposit considerable RF energy on the outboard divertor plate, especially at longer wavelengths. Edge power loss is also occurring due to PDI-generated IBW that drive ions in the edge onto direct loss orbits that intersect the wall, and may be the cause for an observed drag on edge toroidal rotation in combined HHFW and NBI discharges. During plasmas where HHFW is combined with NBI, there is a significant enhancement in neutron rate and fast-ion D_α emission measurements consistent with a strong interaction between the fast-waves and the NBI fast-ions.

Large edge localized modes (ELMs) have been observed immediately following the termination of RF power, whether the power turn off is programmed or due to antenna arcing. RF power has been successfully applied during large ELMs by setting the source reflection coefficient trip levels to relatively high values – an approach potentially important for ITER ICRF heating. Recently the forward and reflected power data has been digitized on some plasmas with microsecond time resolution, rather than with the usual millisecond time resolution. The time derivative of the reflection coefficient obtained from this new high time resolution data is about an order of magnitude larger for an arc than for an ELM and shows that this signal can be used to effectively discriminate between changes in reflection coefficient due to arcs and ELMs.

In 2010 the HHFW research program will use the upgraded antenna, with ELM discrimination system, combined with a new liquid-lithium divertor [35] to study both HHFW+NBI deuterium H-modes and to further develop HHFW heating of the early I_p ramp-up.

ACKNOWLEDGEMENTS

This work would not have been possible without the support of Dr. Masayuki Ono and Dr. Jonathan Menard, the NSTX team and the machine, RF, and neutral beam operations groups. The work is supported by US Department of Energy contracts DE-AC02-09CH11466 and DE-AC05-00OR2272.

REFERENCES

1. M. Ono, *et al.*, *Nuclear Fusion* **41**, 1435 (2001).
2. M. Ono, *Phys. Plasmas* **2**, 4075 (1995).
3. D. W. Swain and R. H. Goulding, *Fusion Eng. Des.* **82**, 603 (2007).
4. P. M. Ryan, *et al.*, *Plasma Physics and Controlled Fusion Research 2002*, Lyon, France (IAEA, Vienna, Austria 2003), paper EX/P2-13.
5. P. M. Ryan, Proc. 35th EPS Conf. on Plasma Physics (Hersonissos, Greece) paper P1.108 (2008).
6. A. P. Smirnov and R.W. Harvey, *Bull. Am. Phys. Soc.* **40**, 1837 (1995).
7. E. F. Jaeger, *et al.*, *Phys. Plasmas* **8**, 1573 (2001).
8. J. C. Hosea, *et al.*, *Phys. Plasmas* **15**, 056104 (2008).
9. C. K. Phillips, *et al.*, *Nuclear Fusion* **49**, 075015 (2009).
10. P. Colestock, *et al.*, *Fus. Eng. Des.* **12**, 43 (1990).
11. H. W. Kugel, *et al.*, *Journal of Nuclear Materials* **390–391**, 1000 (2009).
12. J. C. Hosea, *et al.*, “Recent Fast Wave Coupling and Heating Studies on NSTX, with Possible Implications for ITER”, to be published in Proc. 18th Topical Conf. on RF Power in Plasmas, (Gent, Belgium, June 2009).
13. G. Taylor, *et al.*, “Recent Improvements in Fast Wave Heating in NSTX”, to be published in Proc. 18th Topical Conf. on RF Power in Plasmas, (Gent, Belgium, June 2009).
14. M. Podesta, *et al.*, *Rev. Sci. Instrum.* **79**, 10E521 (2008).
15. R. W. Harvey and M. G. McCoy, Proc. of IAEA Tech. Committee on Advances in Simulation and Modeling of Thermonuclear Plasmas, Montreal, Quebec (IAEA, Vienna, 1993), p. 489; USDOC NTIS Doc. No. DE93002962.
16. D. Liu, *et al.*, “Profiles of Fast Ions that are Accelerated by HHFW in NSTX”, submitted to *Plasma Phys. and Control. Fusion* (2009).
17. V. S. Chan, *et al.*, *Phys. Plasmas* **9**, 501 (2002).
18. M. G. Bell, *et al.*, “Plasma Response to Lithium-Coated Plasma-Facing Components in NSTX”, to be published in *Plasma Phys. and Control. Fusion* (2009).
19. H.Y. Yuh, *et al.*, *Phys. Plasmas* **16**, 056120 (2009).
20. E. Mazzucato, *et al.*, *Nuclear Fusion* **49**, 055001 (2009).

21. B. P. LeBlanc, *et al.*, *AIP Conf. Proc.* **787**, 86 (2005).
22. R. Raman, *et al.*, *Nuclear Fusion* **49**, 065006 (2009).
23. T. M. Biewer, *et al.*, *Phys. Plasmas* **12**, 056108 (2005).
24. J. R. Wilson, *et al.*, *AIP Conf. Proc.* **787**, 66 (2005).
25. G. Chen, *et al.*, "AORSA-1D Simulation of Parametric Decay Instability (PDI) in Tokamak Plasmas" *Bull. Am. Phys. Soc.* **54** Paper CP8.00023 (2009)
26. R. E. Bell, *Rev. Sci. Instrum.* **77**, 10E902 (2006).
27. R. J. Hawryluk, in *Physics of Plasmas Close to Thermonuclear Conditions*, in *Proc. of the International School of Plasma Physics*, (edited by B. Coppi, G. Leotta, D. Pfirsch, R. Pozzoli, and E. Sindoni ~Pergamon, Varenna, Italy, 1981), Vol. 1, p. 19.
28. M. Brambilla, *Plasma Phys. Control. Fusion* **44**, 2423 (2002).
29. W. W. Heidbrink and G. J. Sadler, *Nuclear Fusion* **34**, 535 (1994).
30. M. Nemoto, *et al.*, *Plasma Phys. Control. Fusion* **39**, 1599 (1997).
31. W. W. Heidbrink, *et al.*, *Nuclear Fusion* **39**, 1369 (1999).
32. M. J. Mantsinen, *et al.*, *Phys. Rev. Lett.* **88**, 105002 (2002).
33. A. L. Rosenberg, *et al.*, *Phys. Plasmas* **11**, 2441 (2004).
34. D. Liu *et al.*, *Rev. Sci. Instrum.* **77**, 10F113 (2006).
35. H. W. Kugel, *et al.*, *Plasmas* **15**, 056118 (2008).

FIGURE CAPTIONS**Figure 1**

(a) Comparison of MPTS measurements of electron density in the plasma scrape-off for two similar plasmas, one with lithium conditioning (shot 129254, thick error bars and solid thick line) and one without lithium conditioning (shot 129239, thin error bars and dashed line). Record NSTX core electron temperatures achieved in helium and deuterium plasmas. MPTS measurements of (b) electron temperature and (c) electron density immediately prior to RF heating (0.198 s, dashed line) and during 2.7 MW of $k_\phi = -8 \text{ m}^{-1}$ heating (0.298 s, solid line) of a helium plasma (shot 135260). Laser Thomson scattering measurements of (d) electron temperature and (e) electron density immediately prior to RF heating (0.148 s, dashed line) and during 3.1 MW of $k_\phi = -8 \text{ m}^{-1}$ heating (0.248 s, solid line) of a deuterium plasma (shot 129343).

Figure 2

(Color) (a) Time evolution of the $T_e(0)$, measured by MPTS, for a sequence of deuterium plasmas with $I_p = 600 \text{ kA}$, $B_T(0) = 5.5 \text{ kG}$, 1 MW of RF power starting at 0.15 s, and no Li conditioning. $\Delta\phi$ was adjusted from -30° to 180° in 30° increments between shots. $T_e(0)$ time evolution for a plasma without RF heating (black dashed line) is also plotted for comparison. Note the plasma with $\Delta\phi = -30^\circ$ had an RF arc at 0.22 s. (b) $T_e(R)$ and (c) $n_e(R)$ measured by MPTS at 0.382 s during each discharge shown in Fig. 2(a).

Figure 3

$T_e(0)$ and $n_e L$ evolution measured by MPTS for two similar deuterium L-mode plasmas with 20 mg/min of lithium wall conditioning. Shot 129679 (solid lines) had up to 1.3 MW of $k_\phi = -3 \text{ m}^{-1}$ RF power (shaded region). Shot 129677 (dashed lines) had less than 150 kW of $k_\phi = -3 \text{ m}^{-1}$ RF power.

Figure 4

((a) $T_e(R)$, (b) $n_e(R)$ and (c) $P_e(R)$ measured by MPTS at 0.482 s for two $I_p = 1$ MA, $B_T(0) = 5.5$ kG deuterium plasmas. One plasma had 2 MW of NBI and 1.6 MW of RF power, with $\Delta\phi = 180^\circ$ ($k_\phi = (14 + 18) \text{ m}^{-1}$), from 0.3 to 0.5 s (thick solid line, shot 129386), and the other plasma had 2 MW of NBI from 0.09 to 0.69 s (thin dashed line, shot 129381).

Figure 5

(Color) (a) Time evolution of RF power (blue line), NBI power (dashed green line), plasma stored energy (solid black line) and lower divertor D_α emission (red line) during an $I_p = 1$ MA, $B_T(0) = 5.5$ kG deuterium NBI H-mode plasma with $k_\phi = -13 \text{ m}^{-1}$ heating (shot 130608). The time evolution of the plasma stored energy for a similar plasma, but without RF heating (shot 130609), is shown by the dashed black line. RF power trips off during an antenna arc at 0.375 s and 0.437 s, and is turned off at 0.5 s, in each case there is a large D_α spike associated with a type 1 ELM. (b) Expanded time window around the time of the arc at 0.375 s, and (c) around the time of the RF turn-off at 0.5 s shows the D_α spike associated with the ELM clearly follows the antenna arc and RF turn-off.

Figure 6

(Color) (a) Time evolution of the electron temperature, electron line density, RF and NBI power, and the lower divertor D_a emission during an $I_p = 800$ kA, $B_T(0) = 5.5$ kG deuterium plasma (shot 135340) initially heated by 2 MW of NBI which transitions to an ELMing H-mode during the RF pulse at 0.29 s. This plasma had 2.7 MW of $k_\phi = -13 \text{ m}^{-1}$ heating from 0.25 to 0.46 s. (b) Electron pressure and (c) electron density profiles measured by Thomson scattering just before (0.282 s, blue line) and after (0.298 s, red line) the L-mode to H-mode transition, and at the end of the RF pulse (0.432s, orange line). (d) RF power (black line), RF reflection coefficient (blue line) and lower divertor D_a emission (red line) during shot 135340.

Figure 7

(a) Electron temperature, (b) electron density and (c) electron pressure profiles measured by laser Thomson scattering for two $B_T(0) = 5.5$ kG deuterium plasmas at 0.052 s, during the beginning of the current ramp-up. One discharge has 550 kW of $k_\phi = -8 \text{ m}^{-1}$ heating coupled from 0.02 s (thick solid line) and the other discharge has no RF coupled (thin dashed line).

Figure 8

Anisotropic carbon-III ion heating measured near the plasma separatrix by passive ion spectroscopy. (a) Poloidal ion temperature at a major radius, $R = 1.500$ m and (b) toroidal ion temperature at $R = 1.507$ m, during 1.2-1.3 MW of $k_\phi = -3$ m⁻¹ (thick solid line, shot 129679), $k_\phi = -8$ m⁻¹ (thin solid line, shot 129678), $k_\phi = -13$ m⁻¹ (dashed solid line, shot 129676) RF heating of $I_p = 650$ kA, $B_T(0) = 5.5$ kG deuterium discharges. Also included is a shot with no RF power (shot 129677, dotted line). For the case with $k_\phi = -3$ m⁻¹ heating at 0.444 s, radial profiles of (c) Poloidal (solid line) and toroidal ion temperature (dashed line), and (d) poloidal (solid line) and toroidal (dashed line) carbon-III emissivity. (e) Results from a 1-D full wave model of the daughter IBW amplitude versus pump field and RF power.

Figure 9

(Color) (a) Toroidal velocity of carbon-IV measured at $R = 1.45$ m by CHERS during a short 2 MW NBI at the end of a 1.1 MW RF pulse for the $\Delta\phi = -60^\circ$ to -180° scan shown in Fig. 2. (b) Toroidal velocity of carbon-VI versus major radius for the $\Delta\phi = -60^\circ$ RF heating case shown in Fig. 9(a) and Fig. 2. The edge toroidal rotation appears to clamp during the RF pulse.

Figure 10

(Color) Visible color camera images taken during three $I_p = 1$ MA, $B_T(0) = 5.5$ kG deuterium H-mode plasmas. Image (a) had only 2 MW of NBI heating (shot 130609). Images (b) and (c) had 2 MW of NBI heating and 1.8 MW of $k_\phi = -8$ m⁻¹ heating (shot 130621) and 1.8 MW $k_\phi = -13$ m⁻¹ heating (shot 130608), respectively. The images in frames (b) and (c) were taken at 0.335 s. Image (a) was taken at 0.350 s. An NBI background frame at 0.250 s was subtracted from all three images. (d) Shows the radial heat flux measured by an IR camera viewing the lower divertor plate during two $I_p = 800$ kA, $B_T(0) = 4.5$ kG deuterium H-mode plasmas, one with 2 MW of NBI (shot 135334, dashed black line) and the other with 2 MW of NBI and 2.6 MW of $k_\phi = -8$ m⁻¹ heating (shot 135333, red solid line). There is large rise in heat flux to the outer divertor plate on the shot with RF power.

Figure 11

Power deposition profiles calculated by GENRAY for $I_p = 1$ MA, $B_T(0) = 5.5$ kG deuterium H-mode plasmas with 1 MW of (a) $k_\phi = -8$ m⁻¹ (shot 130621) and (b) $k_\phi = -13$ m⁻¹ heating (shot 130608) predict a broader power deposition at higher k_ϕ .

Figure 12

(Color) (a) Time evolution of a series of short 65 keV NBI blips for two similar $I_p = 800$ kA, $B_T(0) = 5.5$ kG for two similar shots 128742 and 128739. (b) $k_\phi = -8$ m⁻¹ RF heating pulse for shot 128739. (c) Comparison between the measured neutron rates for shot 128739 (RF + NBI, red line) and shot 128742 (NBI, black line), showing enhancement in neutron rate with addition of RF power. (d) FIDA signal versus major radius during the time window between 0.29-0.36 s for three similar plasmas with $k_\phi = -8$ m⁻¹ RF heating and NBI blips (shots 128739, 128740 and 128741, red line and symbols) and a similar plasma without RF heating and only NBI blips (shot 178742, blue line and symbols).

Figure 13

Fast TV camera images showing material being ejected from between the straps at the top and bottom of the HHFW antenna. (a) Image showing strap locations under uniform plasma illumination. The camera view images straps 1 through 9. (b) and (c) shows material being ejected from between straps 7 and 8 at the bottom of the antenna from the top of the antenna between straps 7, 8 and 9.

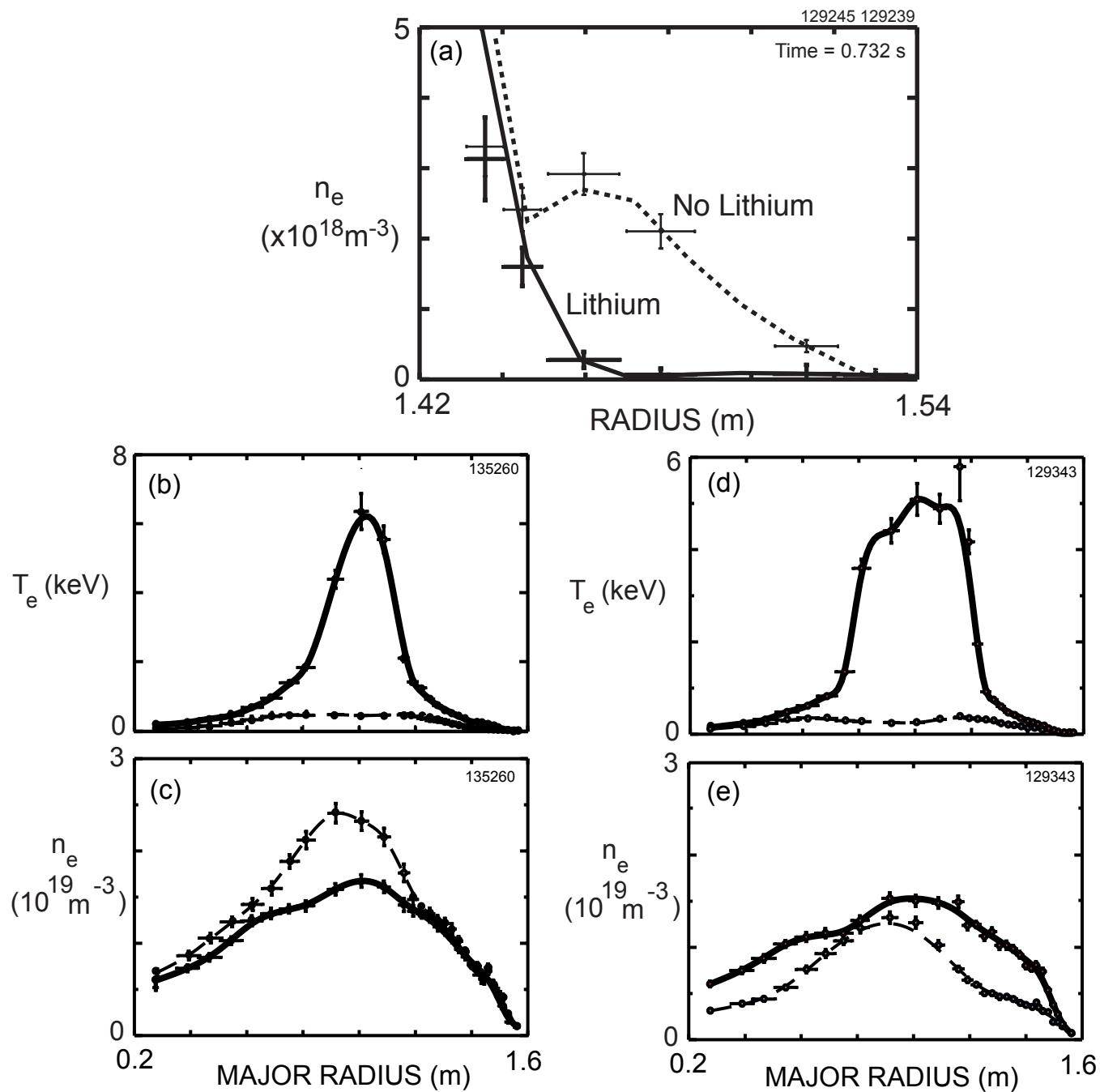


Fig. 1

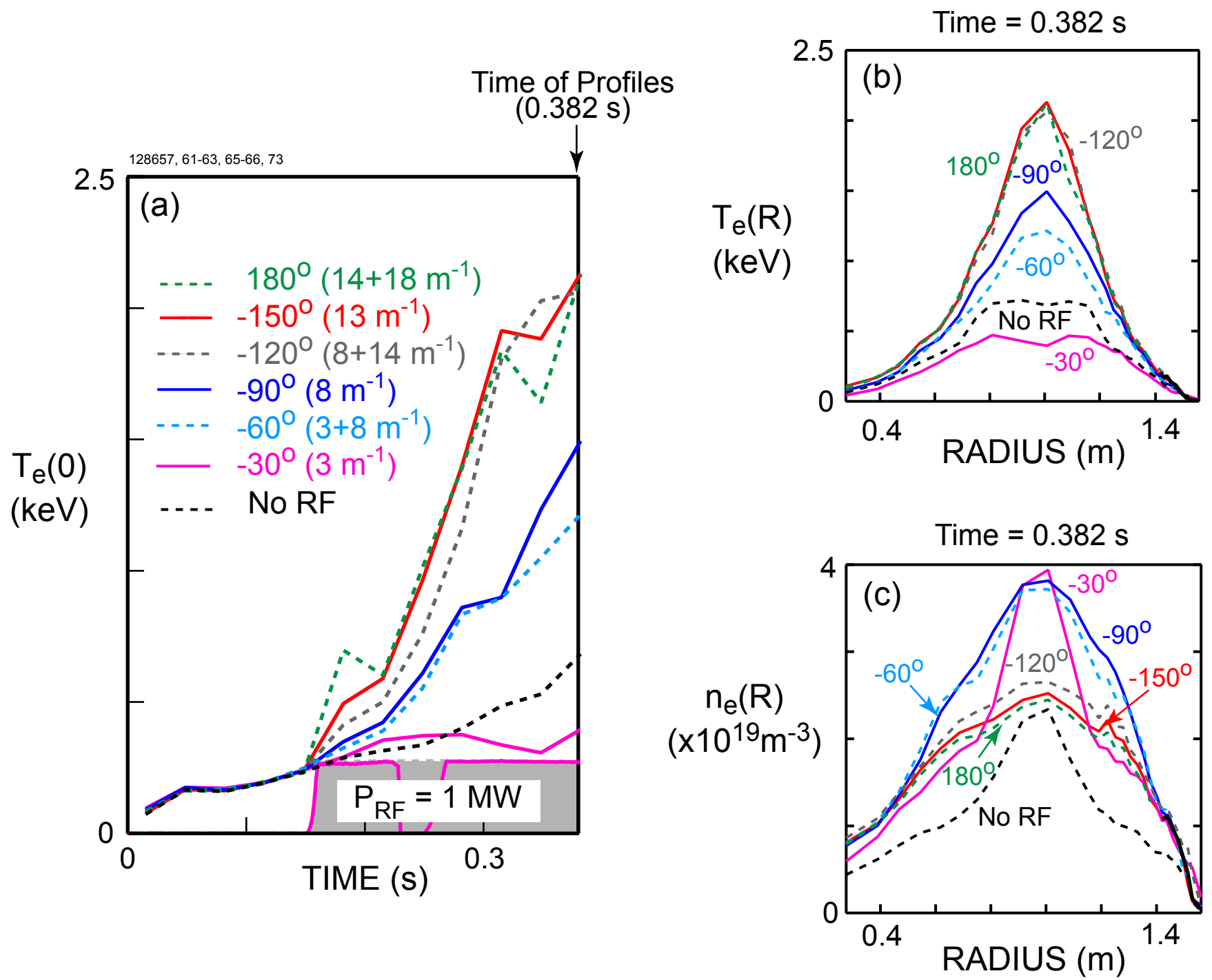


Fig. 2

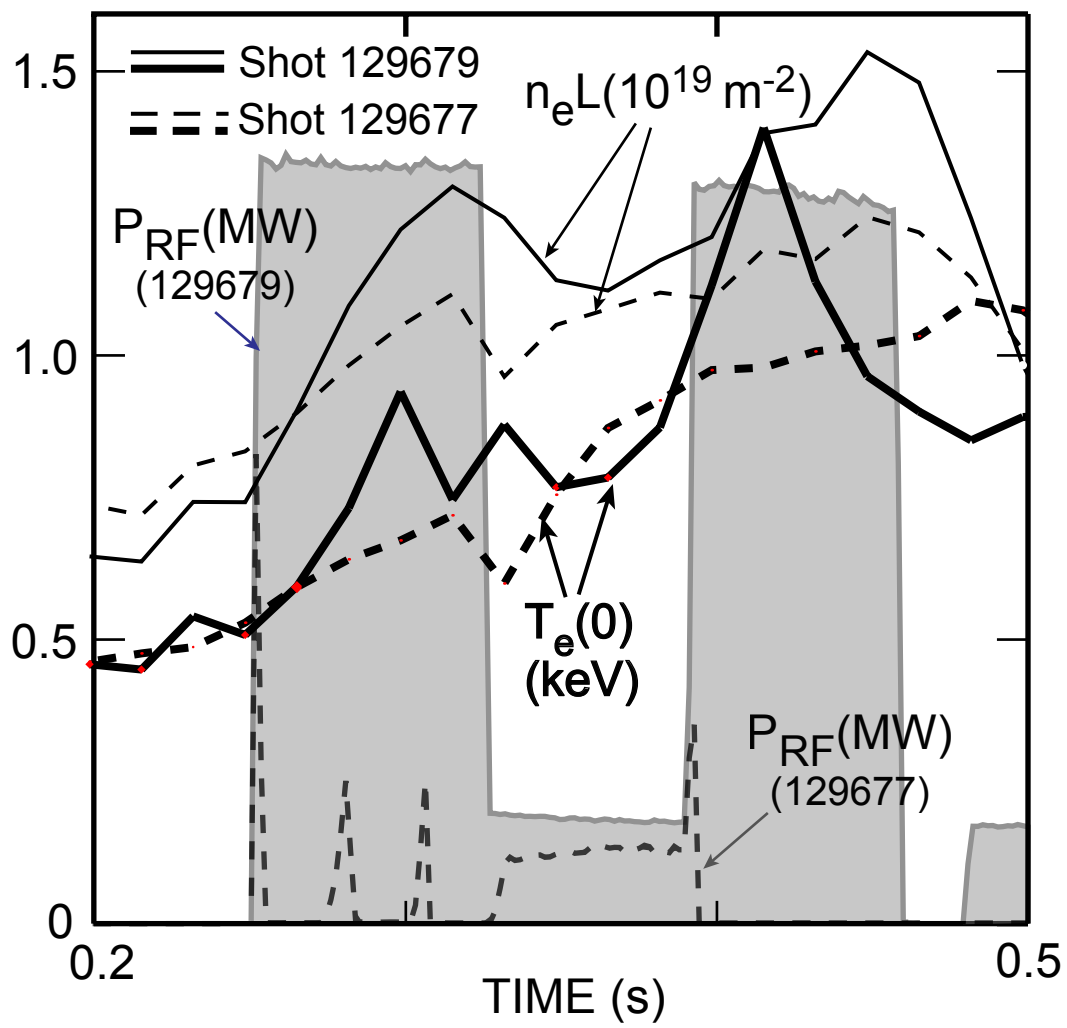


Fig. 3

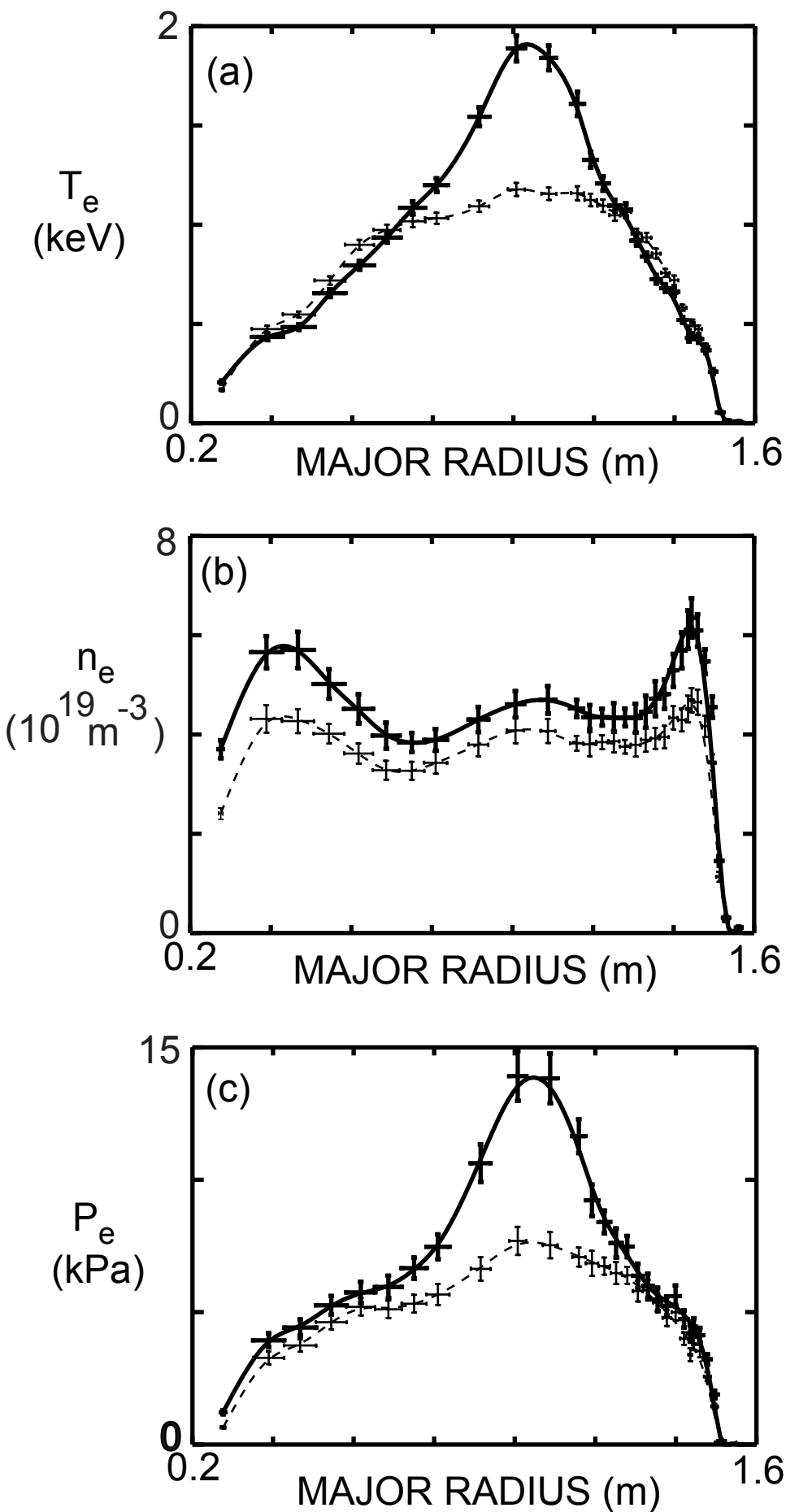


Fig. 4

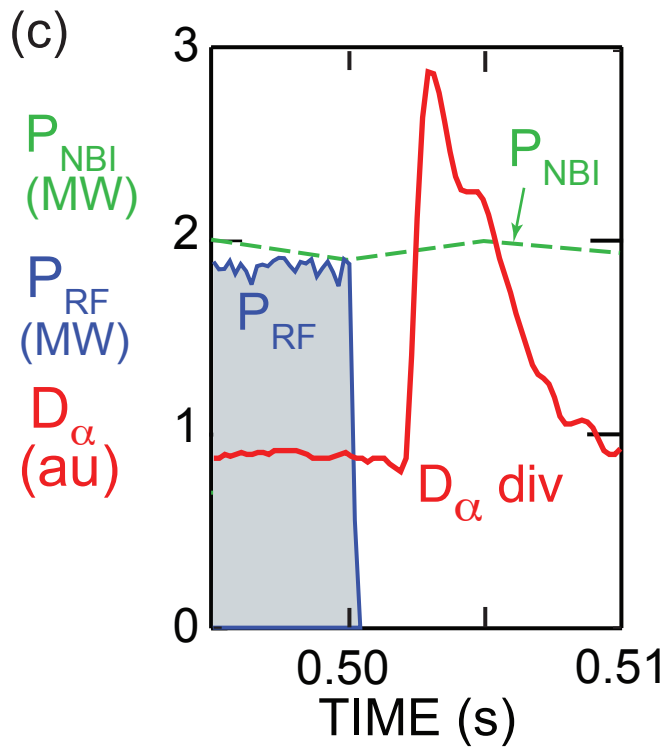
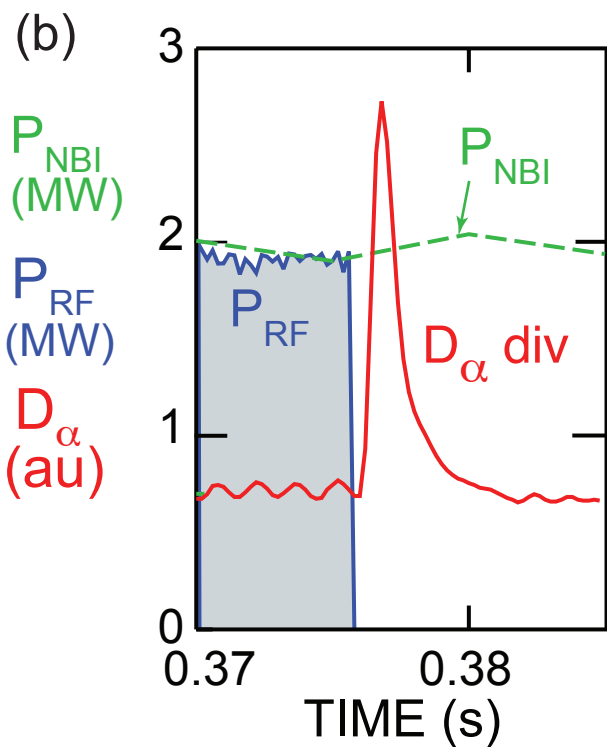
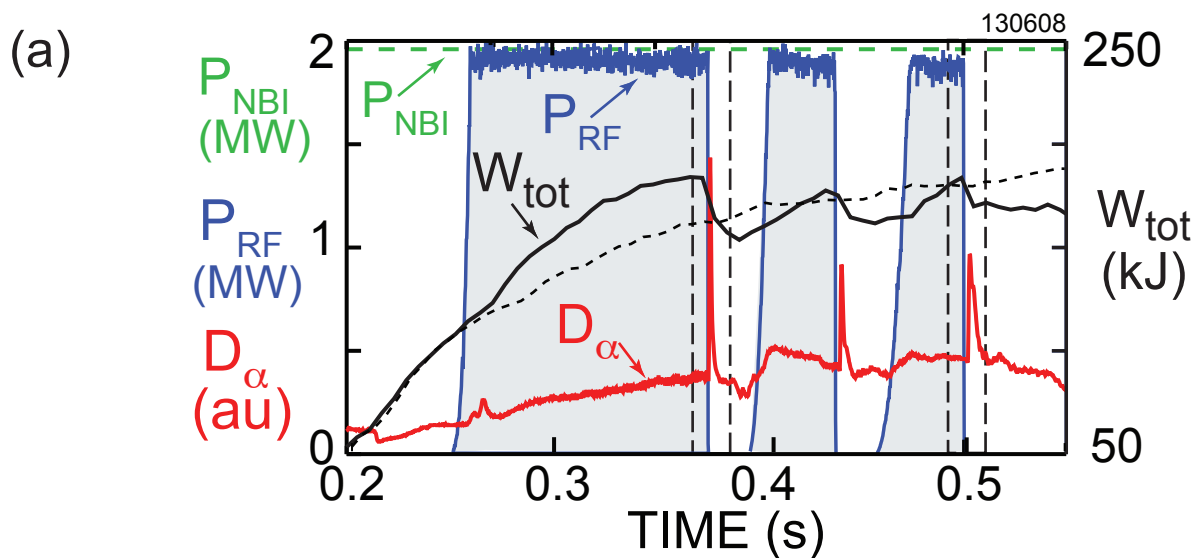


Fig. 5

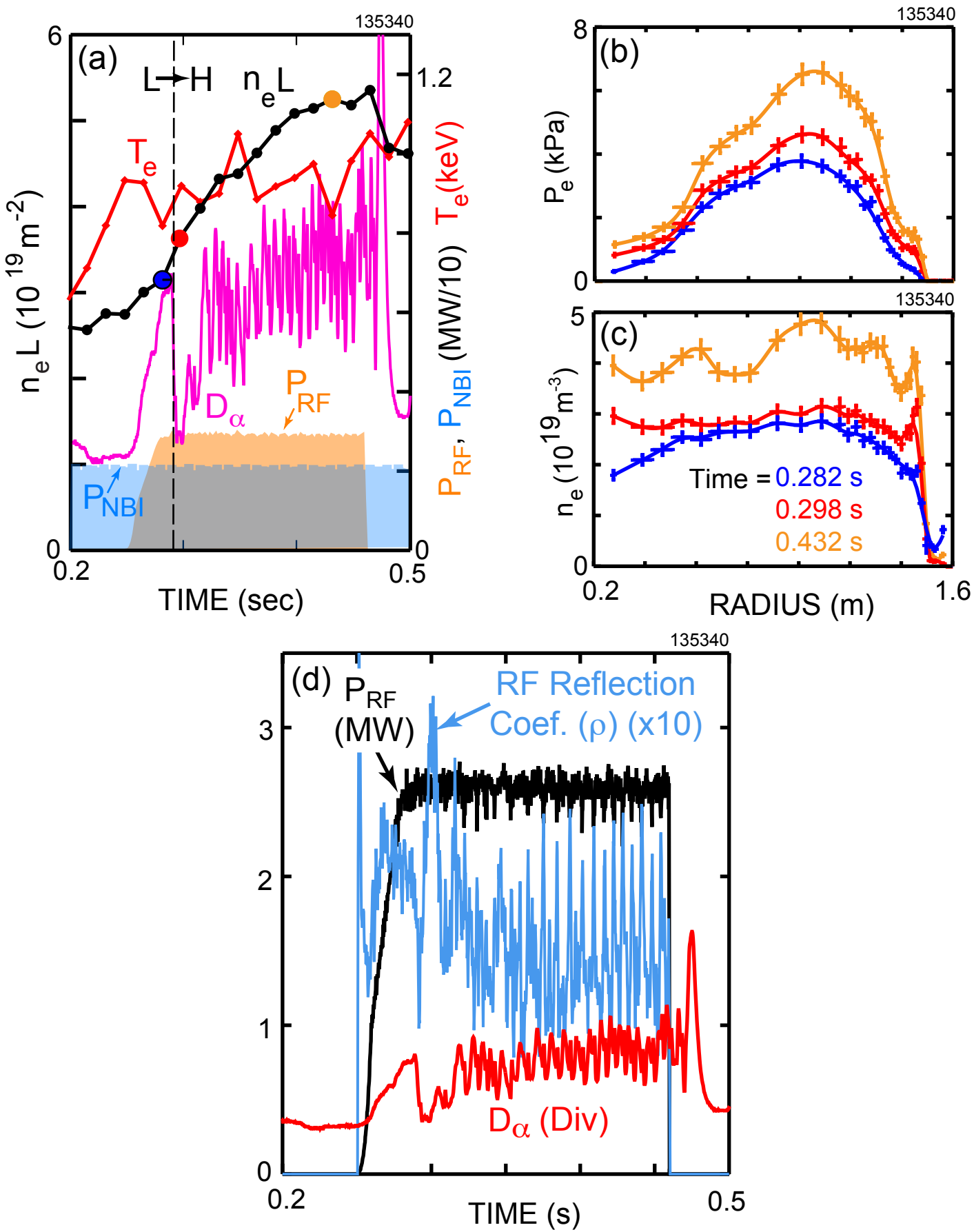


Fig. 6

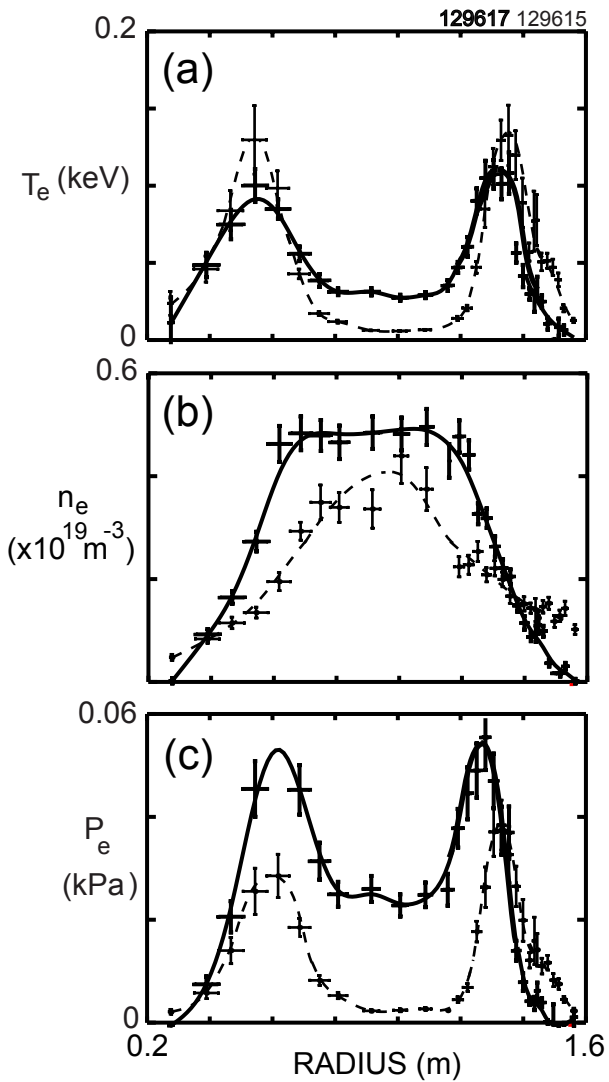


Fig. 7

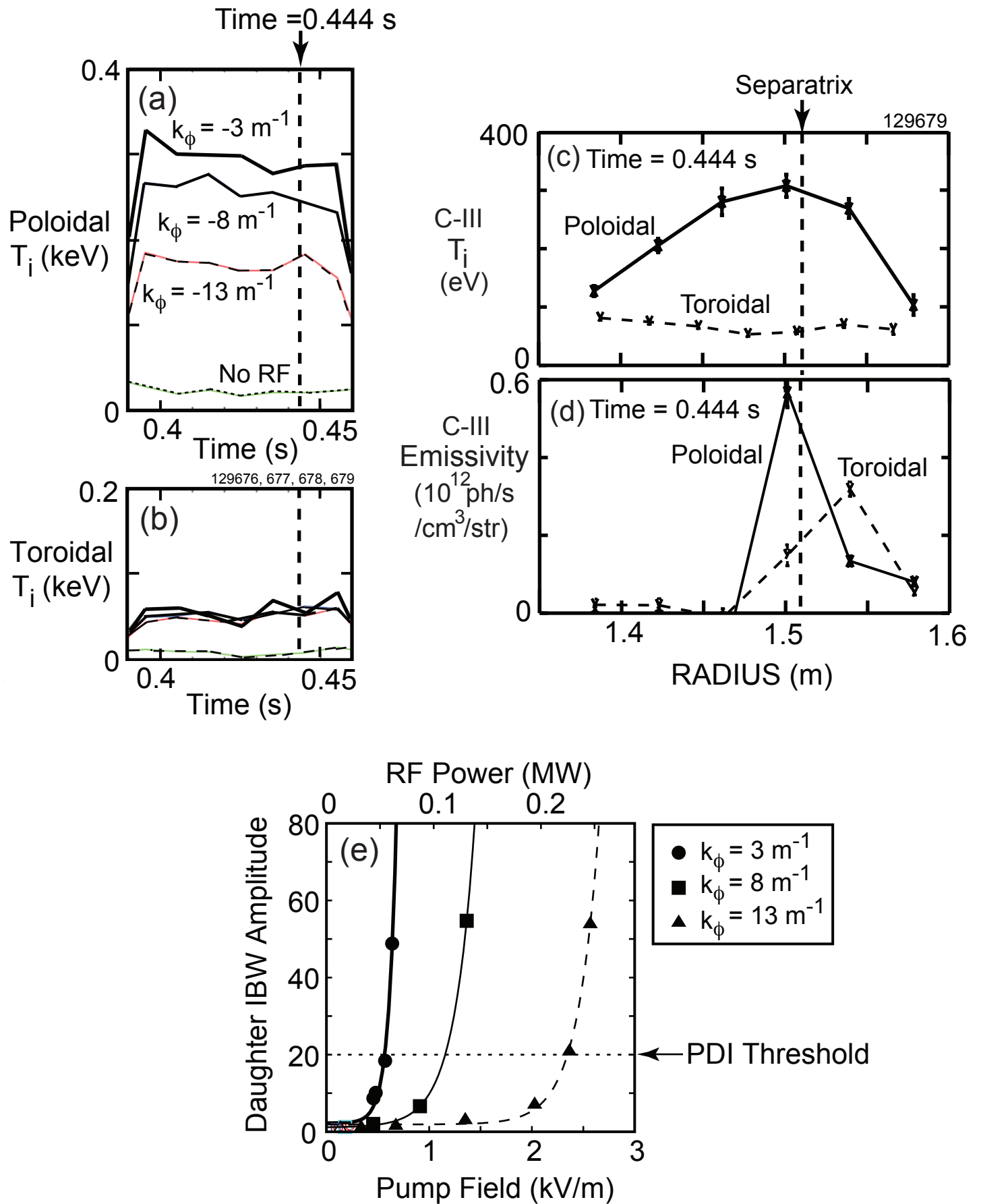


Fig. 8

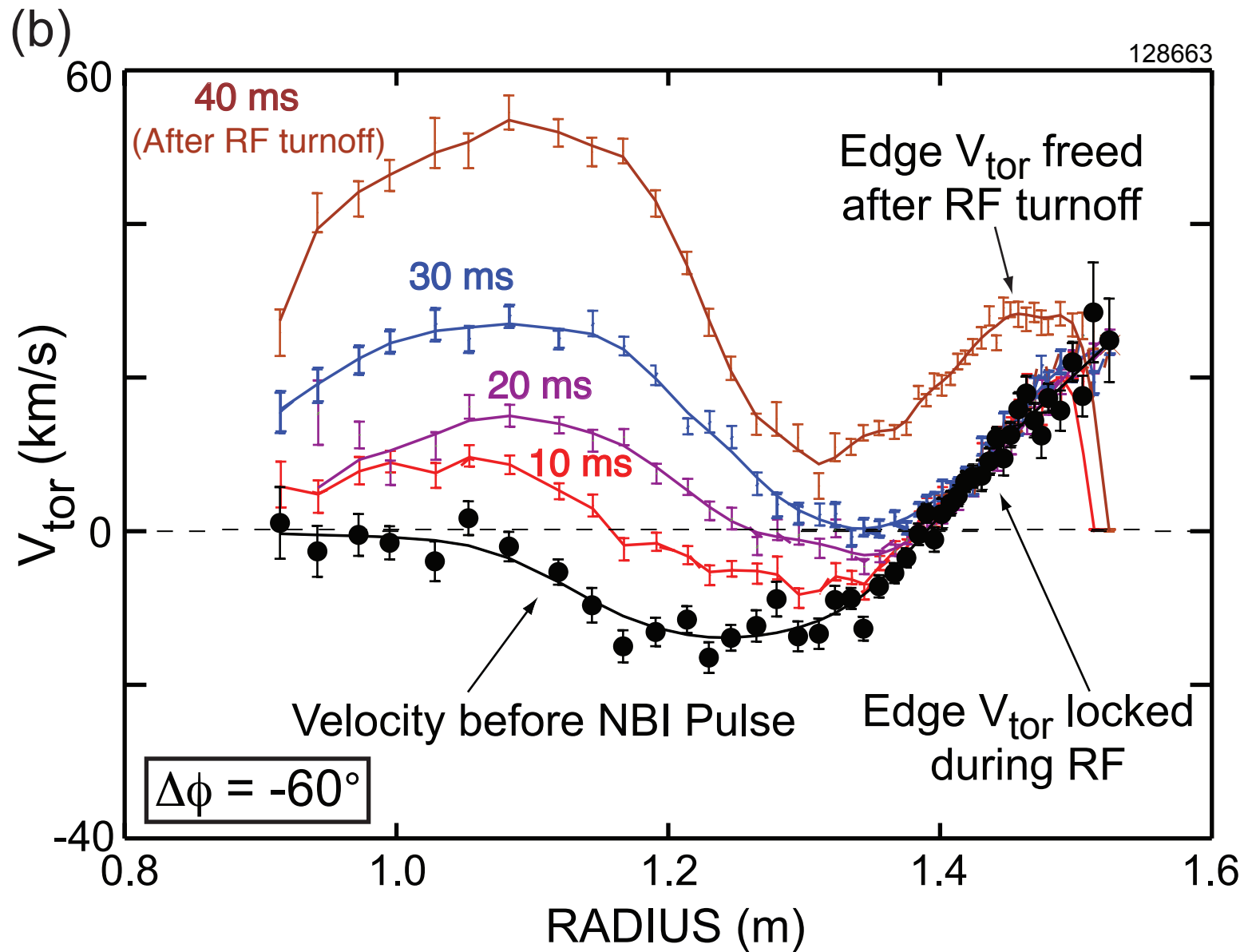
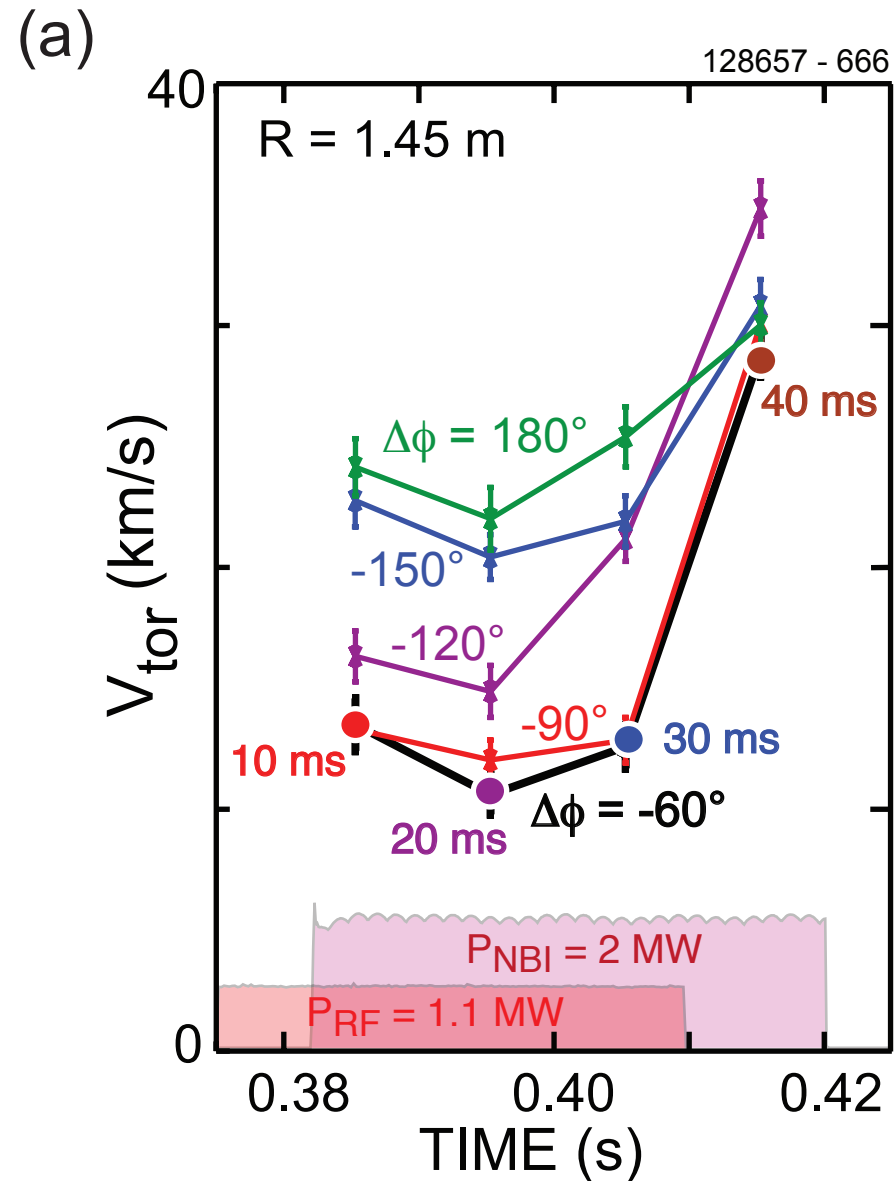


Fig. 9

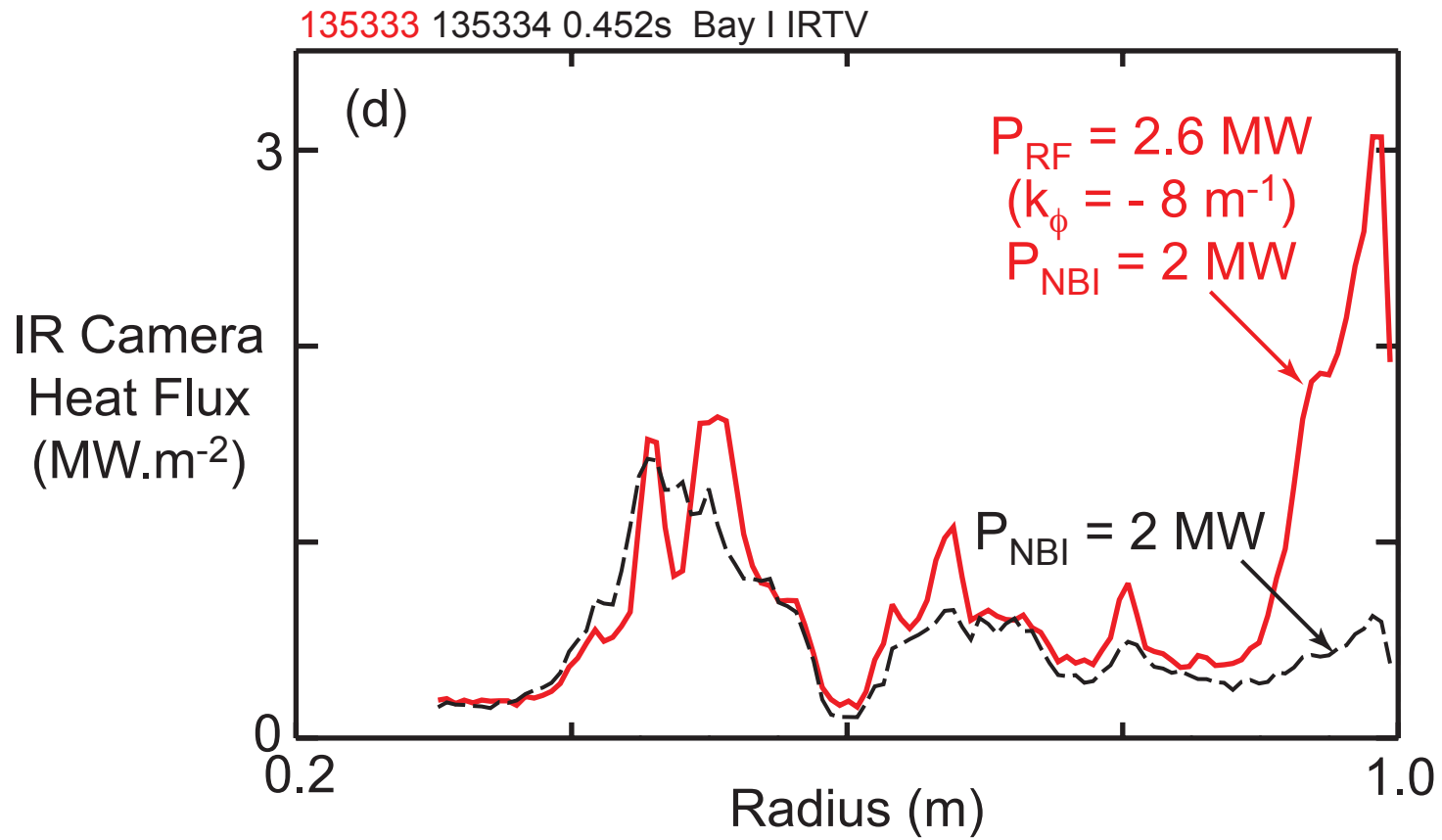
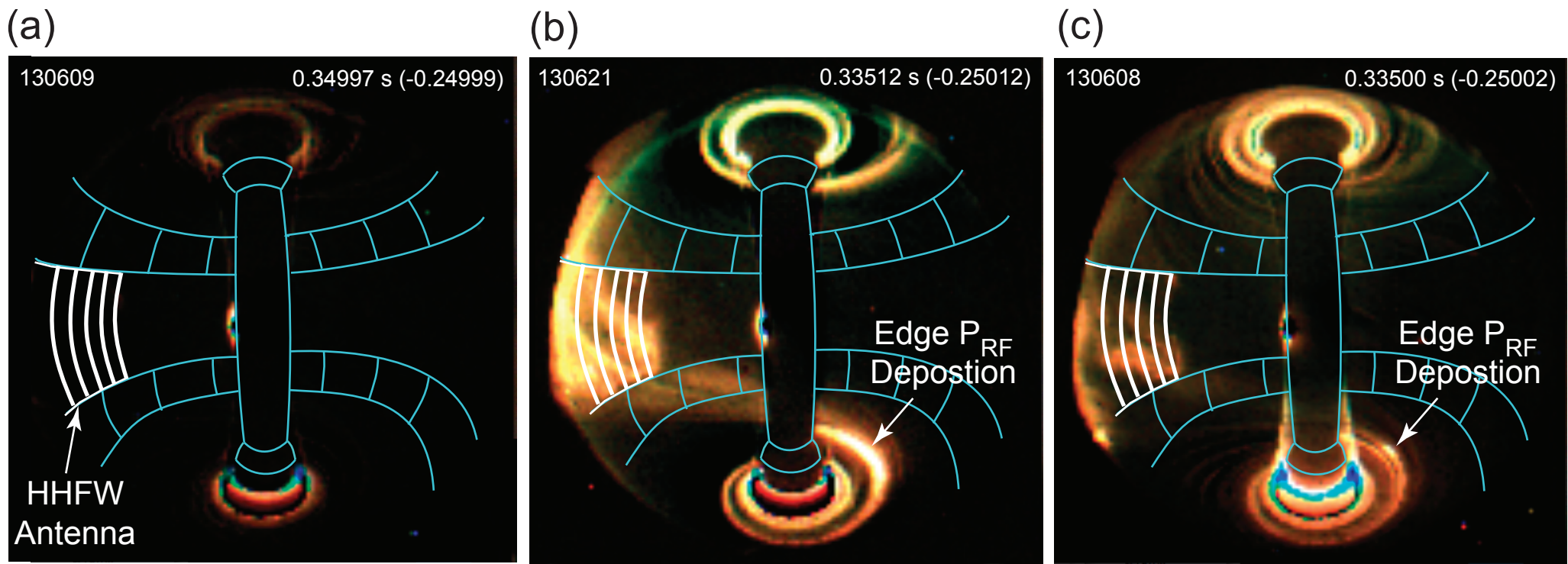


Fig. 10

GENRAY

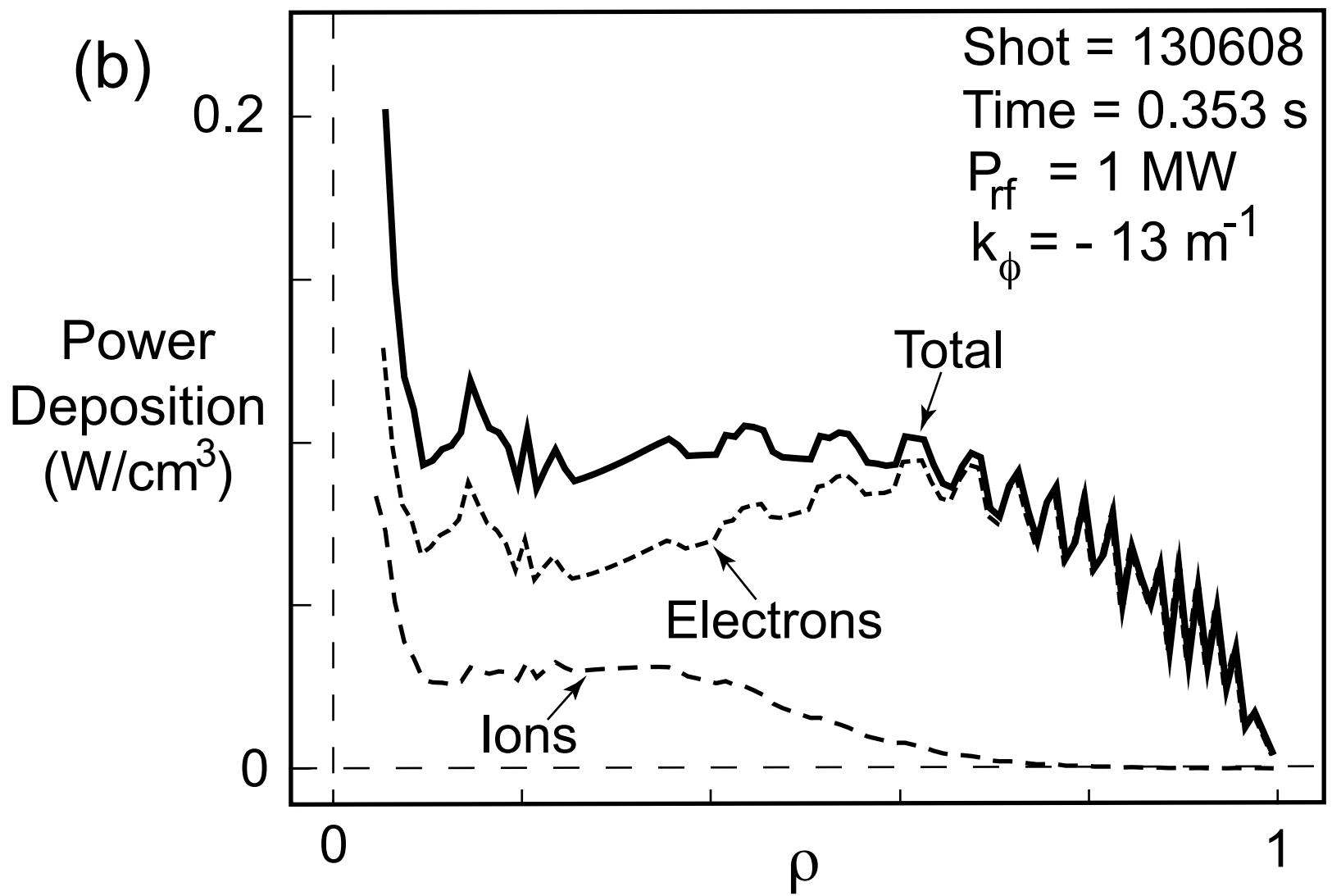
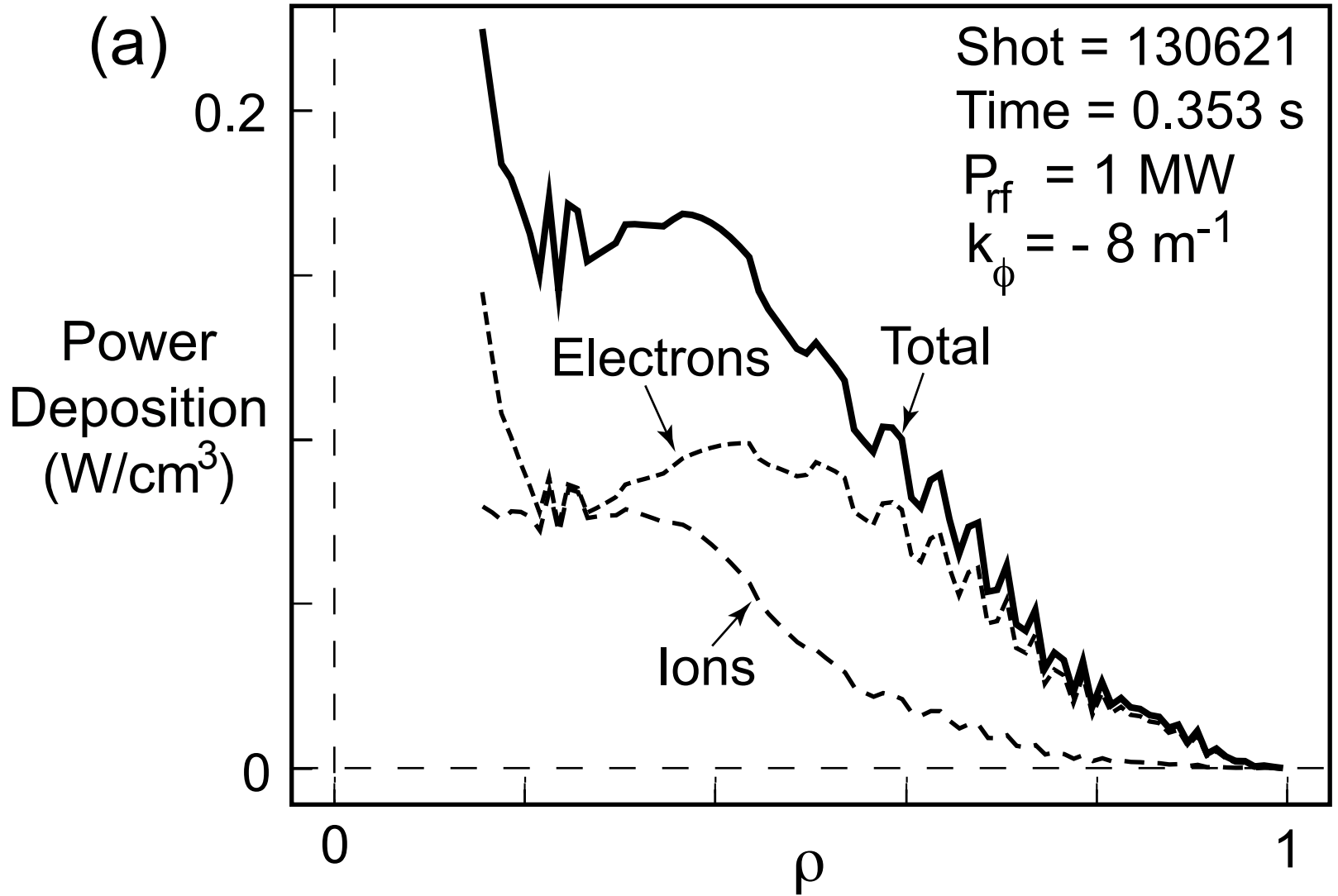


Fig. 11

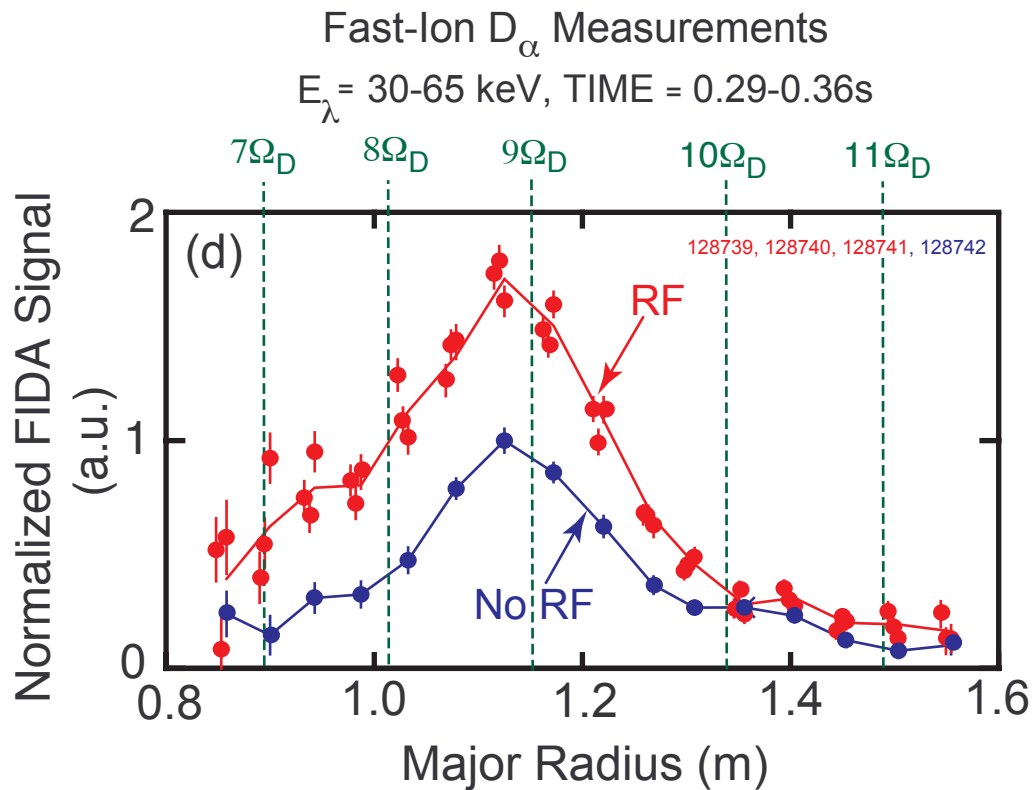
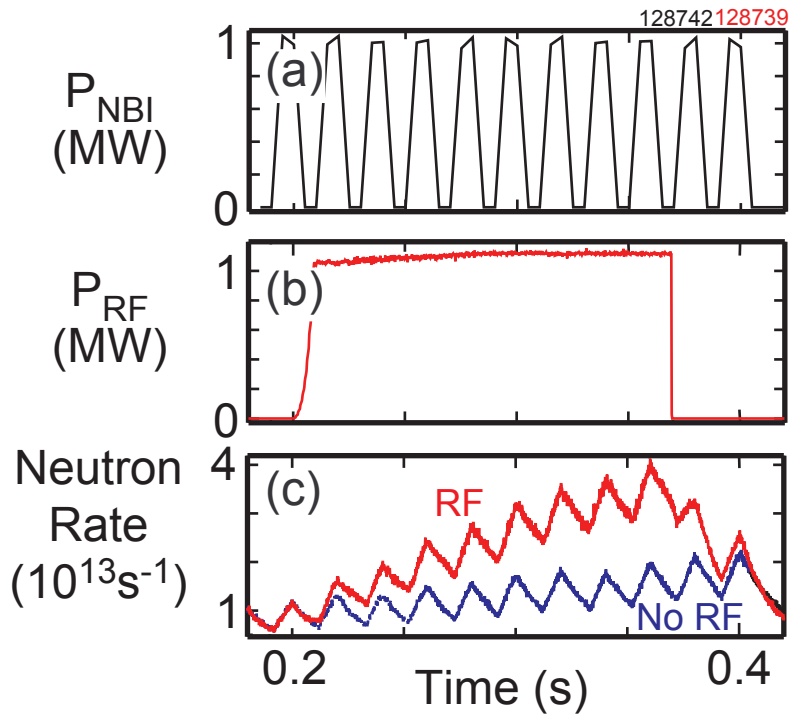
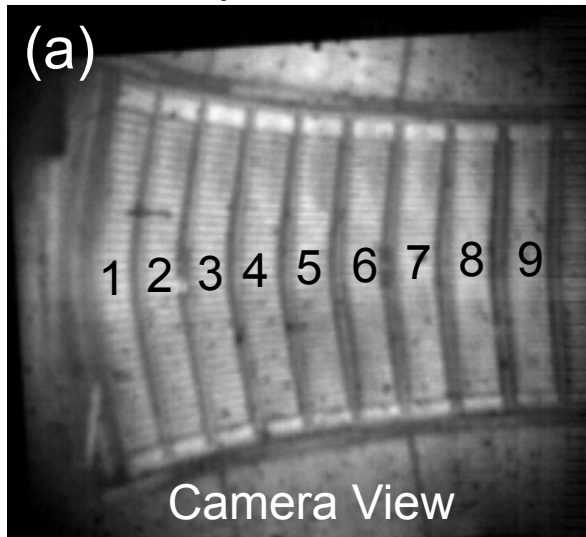
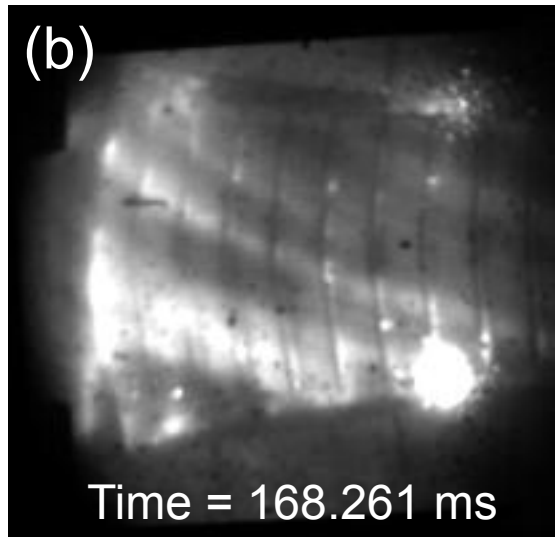


Fig. 12

Strap Locations



Shot 135232



Shot 135232

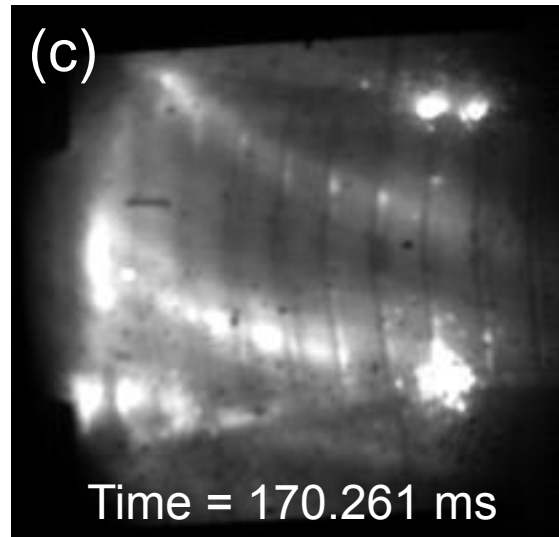


Fig. 13